

Retinal Ganglion Cell Stimulation with an Optically Powered Retinal Prosthesis

William Lemaire¹, Maher Benhouria¹, Konin Koua¹, Wei Tong², Gabriel Martin-Hardy¹, Melanie Stamp³, Kumaravelu Ganesan³, Louis-Philippe Gauthier¹, Marwan Besrou¹, Arman Ahnood⁴, David John Garrett⁴, Sébastien Roy¹, Michael Ibbotson^{2,5}, Steven Praver³, Réjean Fontaine¹

¹ Interdisciplinary Institute for Technological Innovation (3IT), Université de Sherbrooke, Sherbrooke, Quebec, Canada

² National Vision Research Institute, Australian College of Optometry, Carlton, Victoria, Australia

³ School of Physics, The University of Melbourne, Parkville, Victoria, Australia

⁴ School of Engineering, RMIT University, Melbourne, Victoria, Australia

⁵ Department of Optometry and Vision Sciences, The University of Melbourne, Parkville, Victoria, Australia

E-mail: william.lemaire@usherbrooke.ca

Abstract.

Objective. Clinical trials previously demonstrated the spectacular capacity to elicit visual percepts in blind patients affected with retinal diseases by electrically stimulating the remaining neurons on the retina. However, these implants restored very limited visual acuity and required transcutaneous cables traversing the eyeball, leading to reduced reliability and complex surgery with high postoperative infection risks. *Approach.* To overcome the limitations imposed by cables, a retinal implant architecture in which near-infrared illumination carries both power and data through the pupil is presented. A high efficiency multi-junction photovoltaic cell transduces the optical power to a CMOS stimulator capable of delivering flexible interleaved sequential stimulation through a diamond microelectrode array. To demonstrate the capacity to elicit a neural response with this approach while complying with the optical irradiance safety limit at the pupil, fluorescence imaging with a calcium indicator is used on a degenerate rat retina. *Main results.* The power delivered by the laser at safe irradiance of 4 mW/mm² is shown to be sufficient to both power the stimulator ASIC and elicit a response in retinal ganglion cells (RGCs), with the ability to generate of up to 35 000 pulses per second at the average stimulation threshold. *Significance.* This confirms the feasibility of wirelessly generating a response in RGCs with a digital stimulation controller that can deliver complex multipolar stimulation patterns at high repetition rates.

1. Introduction

Around 250 million people in the world are affected with moderate to severe vision impairment caused by uncorrected refractive errors, cataracts, glaucoma and degenerative retinal diseases [1]. Among them, retinal diseases such as age-related macular degeneration and retinitis pigmentosa are particularly difficult to treat due to the complex cellular organization of this sensory membrane. The only currently approved treatment consists in functional neurostimulation to restore visual percepts by electrically stimulating the inner retinal neurons that survive the disease.

Existing clinically approved devices demonstrated the capacity to elicit visual percepts in patients by electrically stimulating the remaining neurons according to an image captured by a camera. They either use an external camera [2] (ARGUS II, Second Sight Inc., Sylmar, California, USA) or an internal photodiode array [3] (Alpha IMS, Retina Implant AG, Reutlingen, Germany) and replicate the image with stimulation pulses on an electrode array surgically affixed to the retina. In both cases, these implants receive power through cables traversing the eyeball. While they enable the generation of visual percepts with neurostimulation, the transcutaneous cables require intricate surgery involving possible complications such as conjunctival erosion, conjunctival dehiscence (reopening of the surgical incision), hypotony (reduction of intraocular pressure) or endophthalmitis (infection) due to the permanent skin penetration [4, 5]. Moreover, the cables can lead to premature failing of the device. In the case of the alpha IMS prosthesis, the median lifetime of the cables was assessed at 1.2 years over 30 implanted first generation devices and at 7.0 years for the second generation [6].

To overcome the safety and reliability limitations induced by the transcutaneous cables, a wireless subretinal implant based on a microphotodiode array was previously proposed [7]. A camera mounted on a pair of glasses captures an image of the visual field and projects it on the retina at high intensity using an infrared projector. The photodiodes directly transduce the infrared image to stimulation pulses on electrodes to which they are individually coupled [8]. The duration and intensity of the projection determine the stimulation pulse widths and currents. Although photodiode array architectures operate fully wirelessly, the direct photodiode amplification mechanism complicates the delivery of stimulation patterns targeted to specific electrodes. In order to produce a stimulation pulse on a particular electrode, the eyeglasses must locate the implant with an accuracy finer than the electrode size at a high refresh rate [9], which can be highly challenging considering the rapid eye saccades and frequent eyeglasses displacements [10, 11]. Although the absence of digital electronics simplifies the design of the implant and minimizes the power consumption, it limits the possibility of dynamically varying some stimulation parameters such as the interphase gap and pulse polarity for selective cell-type stimulation [12]. It also limits the use of active charge balancing [13, 14] and the delivery of flexible multipolar stimulation patterns such as current steering [15, 16] and current focusing [17], which are proven means of enhancing spatial resolution.

In order to provide wireless operation while retaining the flexibility of an implanted digital stimulation controller, we propose an implant architecture that A) receives both power and data through an optical link and B) decouples this link from the stimulation by embedding a digital controller capable of

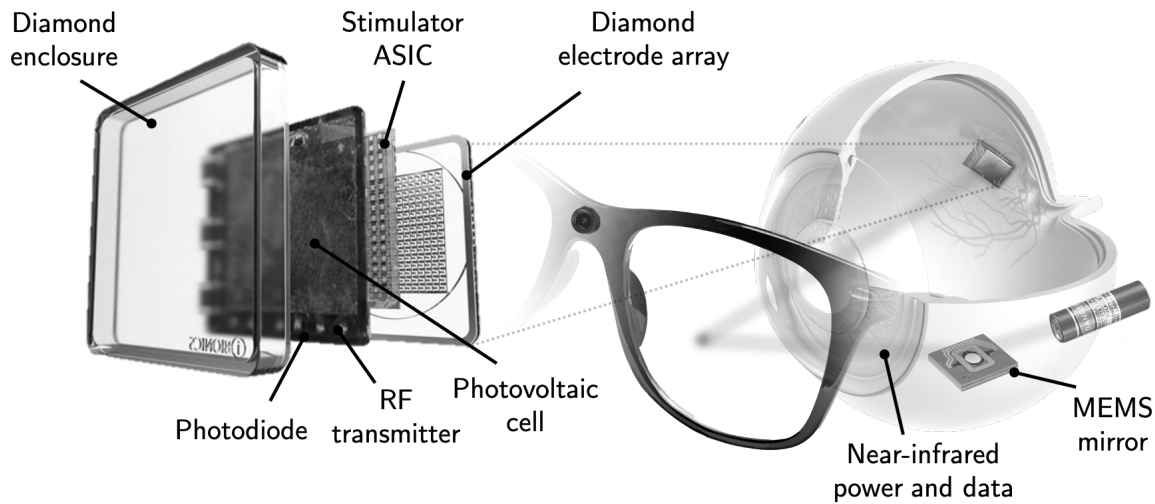


Figure 1. Implant power and data delivery architecture. A MEMS mirror steers an 850 nm laser beam towards the implant. A multi-junction photovoltaic cell captures the infrared light to power a CMOS stimulator ASIC and a photodiode recovers the data from the modulated laser beam. The ASIC delivers the stimulation through an ultrananocrystalline diamond substrate with conductive diamond electrodes.

spatially confined stimulation strategies. To validate the feasibility of this power and data delivery method, a 288 electrode application-specific integrated circuit (ASIC) was designed in TSMC CMOS 65 nm LP [18] and packaged with a multijunction photovoltaic cell for power recovery. Calcium imaging fluorescence microscopy is used to validate that the device can elicit a response on retinal ganglion cells of rats affected by inherited retinal degeneration. Section II presents the implant architecture. Section III presents the materials and methods used to validate the retinal ganglion cells' (RGCs) response. Section IV presents the stimulation results and Section V discusses the implications for future implant design.

2. Implant Architecture

The implant comprises multiple heterogeneous components to allow wireless operation (Figure 1). A high efficiency multi-junction photovoltaic cell recovers the optical power, and a photodiode, with a higher frequency response,

receives the data transmitted by modulating the infrared beam. A stimulator ASIC then decodes the stimulation data, and executes the stimulation pattern on a 288 diamond electrode array. An embedded analog-to-digital converter (ADC) characterizes the electrode properties and sends them back to a radio-frequency (RF) receiver mounted on a pair of smart glasses through a custom-designed RF transmitter. The photovoltaic cell, photodiode, RF transmitter and passive components are assembled on a printed circuit board interposer (Figure 4), which is then mounted on the subassembly comprising the diamond array and the stimulator ASIC (Figure 4). The next section details the rationale behind the design and the choice of each component.

2.1. Photovoltaic Cell

Since the retina is sensitive to temperature increases, the implant power supply is limited by the optical power density that can safely enter the eye. Thermal damage can occur because

of protein denaturation following light absorption in the retinal pigment epithelium. For an 850 nm beam entering the natural or dilated pupil, safety standards for ophthalmic devices dictate that the maximum permissible radiant power is limited to $6.93 \times 10^{-5} C_T C_E P^{-1}$ for chronic exposure at 850 nm, where the wavelength parameter $C_T = 2$ at 850 nm [7, 19, 20]. The pupil factor P models its contraction and dilatation and is equal to one at 850 nm. For spot sizes larger than 1.7 mm in diameter, $C_E = 29.38 \text{ W/mm}^2$. This results in a maximum permissible radiant power density of 4.06 mW/mm^2 that can enter the pupil.

Maximizing the power reaching the implant requires a high efficiency PV cell. Recent photovoltaic cells based on vertical epitaxial heterostructures achieve efficiencies up to 65 % for monochromatic sources [21]. By stacking multiple thin GaAs photovoltaic junctions with submicron absorption thicknesses, it is possible to achieve sufficient voltage for stimulation. The implant is designed around a $3 \times 3 \text{ mm}^2$ photovoltaic cell, resulting in a maximum usable power of 36.5 mW, given the power density limit above. Since redesigning a cell with these custom dimensions requires costly developments, a commercial bare die optical transceiver (Broadcom AFBR-POCXX4L) with dimensions of $1.7 \times 1.7 \text{ mm}^2$ was instead chosen to demonstrate the proposed architecture.

A 15 μF capacitor (C1 in Figure 2) stabilizes the voltage output of the photovoltaic cell and acts as an energy reservoir to complete a stimulation pulse in the event of a power loss during, for example, blinking. The photovoltaic cell connects to the ASIC (Figure 2) through diode D1 (BAS116LP3-7, Diodes Incorporated) to prevent capacitor C1 from discharging into the photovoltaic cell when the laser does not reach the implant, and to pre-

vent the PV cell maximum output of 4.4 V from exceeding the maximum supply voltage of the 65 nm technology.

2.2. Photodiode

In retinal prostheses, wireless data transmission is typically done with an inductive link [22, 3, 23]. However, the bandwidth is generally limited to hundreds of kbit/s and requires a percutaneous cable coupled with a large receiving coil. On the other hand, free-space optical communication can accommodate high data rates with a receiver of minimal complexity and size. The proposed receiving circuit is based on a transimpedance amplifier coupled to a comparator [18] that decodes the data from the photodiode (Albis PDCA04-100-GS). To prevent power variations during transmission and facilitate decoding, the glasses transmit the stimulation scheme using a DC-balanced Manchester code at 2 Mbits/s. The Manchester line code provides a transition in the middle of every bit interval, thus making bit clock recovery trivial at the receiver.

2.3. Stimulator ASIC

The stimulator ASIC is designed in 65 nm CMOS to allow integration of high-density digital circuits. Details about the ASIC are presented in a separate paper [18]. Its architecture (Figure 2) includes 1) 288 electrode drivers, 2) a digital stimulation controller, 3) an optical data recovery circuit, 4) a power management module and 5) an electrode characterization circuit.

2.3.1. Electrode driver To ensure stimulation safety, the electrode driver must provide charged-balanced biphasic pulses. However, in a typical CMOS current source and sink

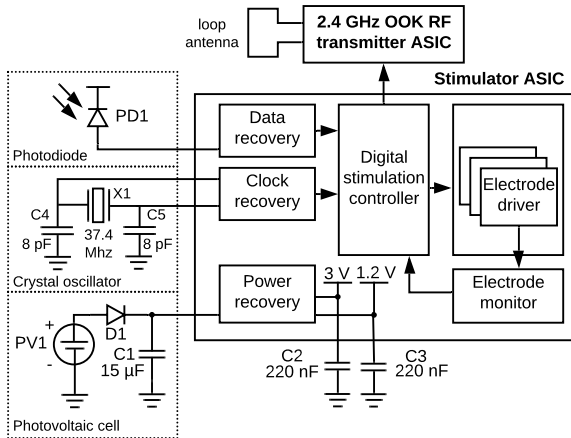


Figure 2. The photovoltaic cell connects to the power recovery block to capacitor C1 to ensure stability. The power recovery module linearly regulates the voltage to 3 V for the electrode drivers and 1.2 V for digital circuits. The clock recovery circuit provides a 935 kHz clock to the digital stimulation controller and a 37.4 MHz clock to the data recovery to oversample the Manchester-encoded data. From this recovered data, the digital stimulator ASIC sequences the pulse train for the electrode driver. The electrode monitor records the voltage at the output of any electrode driver and sends it out through the custom 2.4 GHz RF transmitter.

pair, the process variations will unbalance the cathodic and anodic currents. To prevent this, the ASIC uses a dynamic current copy architecture. It operates with a calibration phase where the current sink driver sets the current that flows through the current source driver. The current source driver then copies that current and stores the calibration, corresponding to the gate-source voltage of the transistor, on a capacitor. [24, 25]. The electrode driver can provide pulse widths ranging from 10 μ s to 700 ms in steps of 10 μ s and with amplitudes from 50 μ A to 255 μ A in steps of 1 μ A with a voltage range of up to ± 2.7 V.

2.3.2. Digital stimulation controller One of the key requirements for the stimulator ASIC is to provide flexible stimulation patterns. Moreover, because the optical power delivery can be interrupted by an eye blink, the implant must also be able to restore stimulation quickly after power up. Some implantable ASICs require a configuration phase and a stimulation phase [25], and in the event of a power failure, this implies that the device must be reprogrammed before stimulation can resume. The digital stimulation controller operates in a stateless fashion, where each new frame fully configures the next stimulation pulses (phase durations, currents, and selection of active and return electrodes). Thus, as soon as the power is reestablished, the stimulation resumes its operation without the need for bidirectional communication.

2.3.3. Electrode monitor The characterization of electrode impedance enables adaptation of the stimulation to the available voltage dynamic range. To achieve this, any given electrode can be selected via a multiplexer for connection to a 8-bit ADC. To allow the waveform measurement of short pulses on the order of tens of μ s, it digitizes the voltage of the stimulation pulse at a maximum sampling rate of 90 kHz.

2.3.4. Power, data and clock recovery The power recovery block linearly regulates the PV cell power to 3.0 V for the electrode driver and electrode monitor circuits and to 1.2 V for the digital circuits. Having two different voltages allows greater stimulation headroom while minimizing the power consumption of digital circuits. The clock recovery circuit generates the clock from the 37.4 MHz crystal, and divides it by 40 to provide a 935 kHz system clock. The data recovery

circuit uses a transimpedance amplifier to recover the Manchester-encoded data from the photodiode, and oversamples it with the 37.4 MHz clock. Oversampling enables maximum energy transfer from the received bit and straightforward bit clock recovery (no phase-locked loop) to minimize power consumption.

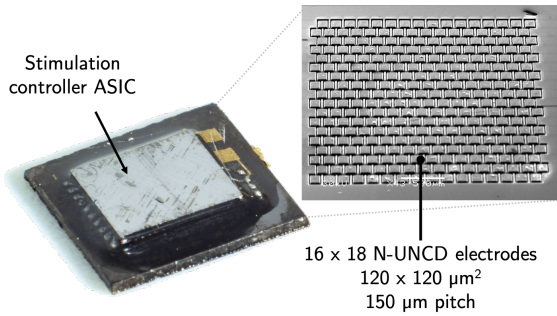


Figure 3. The stimulator ASIC is assembled on the diamond substrate with solder bumps to connect to each of the 288 electrodes.

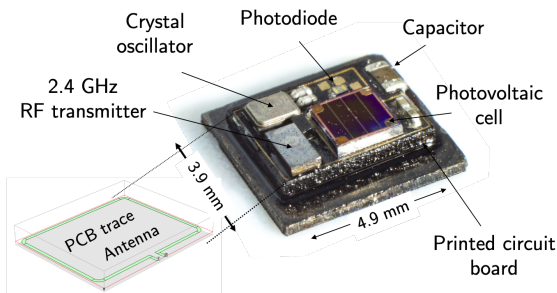


Figure 4. The photovoltaic cell, photodiode, crystal oscillator and RF transmitter are assembled on a 2-layer FR4 printed circuit board. A copper trace antenna surrounds the components. The printed circuit board is assembled on the diamond substrate (Figure 3).

2.4. Diamond Electrode Array and Package

The packaging and electrode design of retinal implants is critical to ensure reliability while immersed in a biological fluid environment. The Argus II implant was enclosed in a fully

hermetic package, with one cable connection to each of the 60 platinum-gray electrodes. Within three years of operation, 29 out of 30 implants were still functioning [5]. However, an implant with a significantly higher electrode count would require an excessive amount of feedthroughs with this approach. Instead, the Alpha IMS device generates stimulation waveforms directly on the pads of its CMOS chip, which are coated with iridium oxide (IrOx). Since this approach precludes the use of a hermetic enclosure, the device is instead encased in conformal coating to minimize corrosion. Without a hermetic enclosure, the median lifetime of the CMOS chip was assessed at 1.22 years [6].

Another possible failure mode is the electrode material degradation. Iridium Oxide and platinum electrodes are often used due to their adequate charge injection capacity and impedance for retinal stimulation. However, these materials are deposited as a coating and can be subject to delamination [26]. Alternatively, ultrananocrystalline (UNCD) diamond can be made conductive with the co-deposition of a dopant (boron) and the inclusion of nitrogen during its production by chemical vapor deposition (CVD). This electrode material provides sufficient charge injection capacity for stimulation and while allowing non-conductive and conductive diamond to coexist in the creation of a monolithic package comprising both the enclosure and the electrodes [27, 28, 29].

Using this method, a 16×18 diamond electrode array was designed with $120 \times 120 \mu\text{m}$ square electrodes separated by a pitch of $150 \mu\text{m}$ on which the stimulator ASIC was assembled. However, to facilitate the calcium imaging experiments, the stimulator ASIC and components were assembled on a printed circuit board, and connected with wires to a 5×5 electrode diamond array with

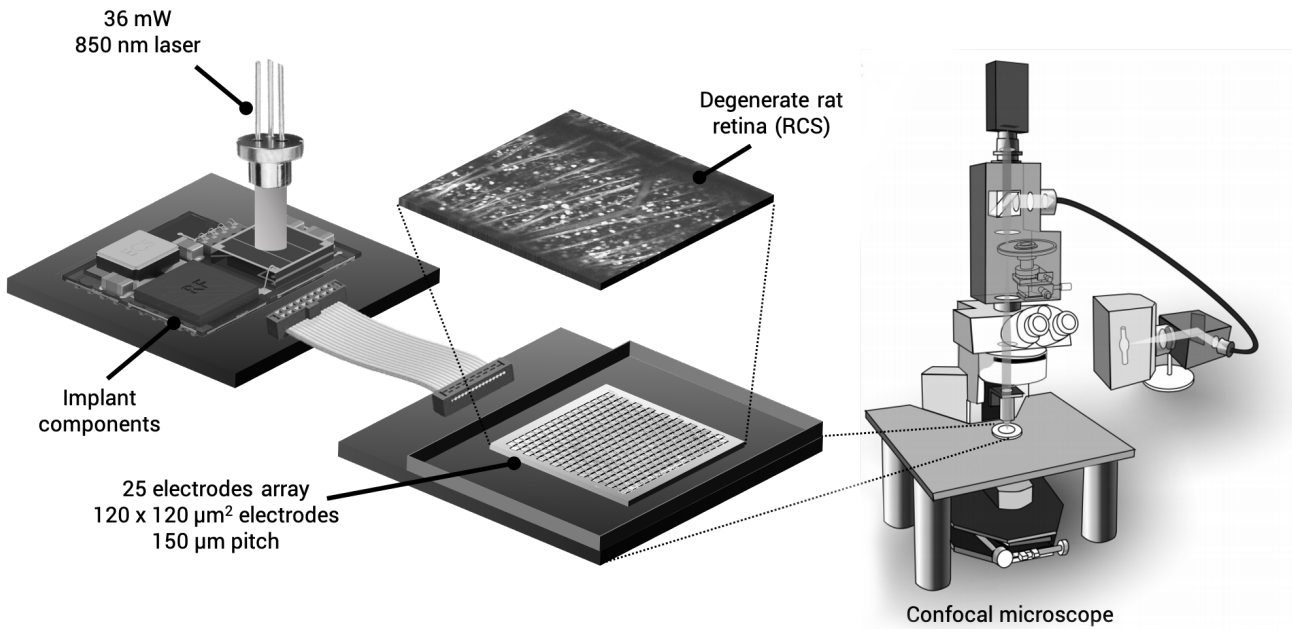


Figure 5. To validate the implant powering method using laser illumination, an apparatus was designed to facilitate calcium imaging where the implant components are assembled on a printed circuit board. A 35 mW, 850 nm laser powers the implant. A cable connects the implant to a 5×5 electrode array. A degenerate rat retina stained with a calcium indicator is placed on the electrode array with retinal ganglion cells facing up. The RGCs's response is evaluated by measuring rapid fluorescence variations with a confocal microscope.

the same pitch and electrode dimensions. The fabrication of the diamond array is presented in a separate paper [30].

2.5. Printed Circuit Board Interposer

In the final implant, the photovoltaic cell, crystal oscillator, PV cell and RF transmitter are assembled on a high density printed circuit board (Figure 4). The FR-4 printed circuit board (PCB) comprises 4 layers, with dimensions of $3.9 \times 4.9 \text{ mm}^2$ and a thickness of 1.6 mm. A copper trace surrounds the PCB and forms the RF antenna. For the actual implant, this PCB would then be affixed to the diamond substrate (Figure 3). For the calcium imaging experiment, the implant was physically separated from the diamond substrate and connected with a cable because the stack height of the laser diode, optics and implant was too high to be placed under the

confocal microscope.

2.6. RF Transmitter and Antenna

Due to power and area limitations, it is necessary to minimize the complexity of the implanted RF transmitter and antenna and relocate the complexity at the receiver side where there are less constraints. A typical oscillator-based transmitter requires multiple internal RF submodules and external components. To minimize the complexity, the transmitter operates from a simpler complementary cross-coupled LC oscillator architecture at 2.4 GHz (Fig. 6). An internal on-chip capacitor and a loop PCB antenna inductor compose the LC resonant network. Since the resonant frequency changes with fabrication variations, the on-chip capacitor is digitally tunable to adjust the frequency. The transmission efficiency at higher frequencies of

2.4 GHz allows a good compromise between tissue losses and loop antenna efficiency, although the efficiency is expected to be significantly lower in a biological environment than in air [31].

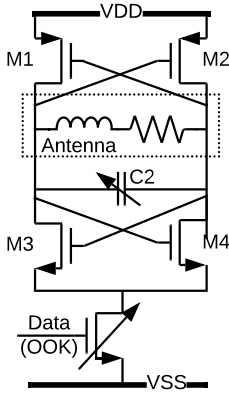


Figure 6. Complimentary cross-coupled LC oscillator architecture of the RF transmitter. The PCB loop antenna is modeled by a resistor and an inductor.

The transmitter supports both on-off keying (OOK) and frequency-shift keying (FSK) modulations. In OOK mode, transistor M5 switches the oscillator according to the serial data stream. In FSK mode, the oscillator is maintained active and the frequency is modulated using tuning control signals for the on-chip capacitor. Transmission power is adjustable by gating the width of M5 to control the current passing through the cross-coupled pair. The transmitter is implemented in 65 nm GP technology with a die size of $0.7 \times 1.5 \text{ mm}^2$ and an active area of $30 \times 60 \text{ }\mu\text{m}^2$. The power consumption varies from 0.2 mW to 0.5 mW during transmission depending on the selected transmission power.

Antenna design for implantable transmitters generally involves a compromise between the transmission efficiency and dimensions. Due to the surgery constraint, the physical antenna size must be much smaller than its

radiating wavelength at 2.4 GHz. With side dimensions of a few millimeters, the loop antenna can be modeled as an inductor in series with a resistor. The antenna dimensions and materials allow to estimate its characteristics. The antenna was fabricated with dimensions of $3.1 \times 4.1 \text{ mm}^2$ (Fig. 4) with a 0.076 mm, 0.5-oz copper trace on a 1.6 mm FR-4 printed circuit board. These parameters result in a simulated inductance of $L = 12 \text{ nH}$ at 2.4 GHz. To allow tuning the frequency between 2.2 and 2.6 GHz, the internal capacitor is adjustable adjustable between 310 fF and 440 fF.

3. Materials and Methods

To validate the proposed wireless power and data delivery architecture, the neural response of degenerate rat retinas to electrical stimulation from a single electrode was measured with calcium imaging. Then, the implant power consumption budget is determined to evaluate the headroom for delivering complex stimulation patterns comprising multiple sequential pulses.

3.1. RGCs Response to Wireless Stimulation

The response of retinal ganglion cells under wireless stimulation is evaluated by generating spatial threshold maps of retinal ganglion cells around a single electrode. A map is realized for short pulse widths of 100 μs and for longer pulses of 500 μs to replicate a typical configuration used by the first generation of retinal implants [32]. The next subsections details how the spatial threshold maps are realized.

3.1.1. Implant test bench To deliver the stimulation pulses, the stimulator ASIC, photodiode, photovoltaic cell, crystal and

passive components (C1, C2, C3, D1 from Figure 2) are assembled on a printed circuit board (Figure 5). Then, the electrode driver pads are connected with cables to a 5×5 electrode array assembled on a second printed circuit board. The power and data is sent to the implant using an 850 nm laser diode (L850P200, Thorlabs). The output power of the laser diode is adjusted by the laser driver (iC-NZ, iC-Haus Inc.) with a power meter to 35 mW. An ADRV9364-Z7020 System-on-Module controls the laser driver to encode the stimulation data with a binary amplitude shift keying (BASK) scheme.

3.1.2. Retina preparation Retina preparation is performed in accordance with the ethical protocol of the Animal Care and Ethics Committee of The University of Melbourne. Adult Royal College of Surgeons (RCS-p+) rats of either gender and older than 3 months are prepared. RCS rats have inherited retinal degeneration which causes their retina to lose most of its photoreceptors by 90 days after birth [33].

The retina is injected with a fluorescent indicator dye through the optic nerve for calcium imaging. The dye is Oregon Green 488 BAPTA-1 solution (OGB-1, Hexapotassium salt, Thermo Fisher Scientific, dissolved in deionised water). The retina preparation and calcium indicator loading is described in detail in a separate paper [30].

The retina is mounted on the diamond electrode array with the ganglion cell layer facing up and held with a steel harp fitted with Lycra threads (SHD-25GH, Warner Instruments). The diamond array is assembled on a printed circuit board which constitutes the bottom of a 3D printed perfusion chamber. The chamber is perfused with a carbogenated Ames' solution at a rate of 3-8 mL/min held

between 35°C and 37°C. The electrode array is kept around 2.5 mm away from the optic nerve.

Although the implant is designed to be placed epiretinally, the electrode array is placed subretinally in this demonstration to facilitate the experiment with calcium imaging. For maximum light transmission to an upright microscope, the retinal ganglion cells need to face the top of the microscope. Thus, the electrode array is placed on the bottom face (subretinally) in order to avoid obstructing the line of sight of the microscope.

3.1.3. Calcium imaging The retina preparation is imaged with a confocal microscope (Olympus FluoView FV1200) with a 10× and a 20× lens, for a field of view of either $318 \times 318 \mu\text{m}^2$ or $633 \times 633 \mu\text{m}^2$. The calcium dye is excited with a 473 nm source, and images are captured at a rate of 7.8 Hz.

3.1.4. Electrical stimulation The electrical stimulation is delivered by the ASIC and consists of charge balanced, biphasic current-controlled pulses. The pulses are delivered with an anodic-first polarity, with phase durations of 100 μs and 500 μs with a 10 μs interphase gap. The dynamic current copy architecture of the stimulation drivers requires a calibration phase prior to the stimulation whose duration is set to 30 μs . The stimulation protocol is detailed in Figure 7. An Ag—AgCl wire acts as the return electrode and is placed in the perfusion chamber, 2 cm away from the stimulating electrodes.

3.1.5. Data analysis Electrical responses are evaluated by identifying rapid temporal changes in the fluorescence image. To achieve this, the response is evaluated by filtering the signal of each pixel with a temporal high-pass filter (with coefficients [2,1,-1,-2]), and then

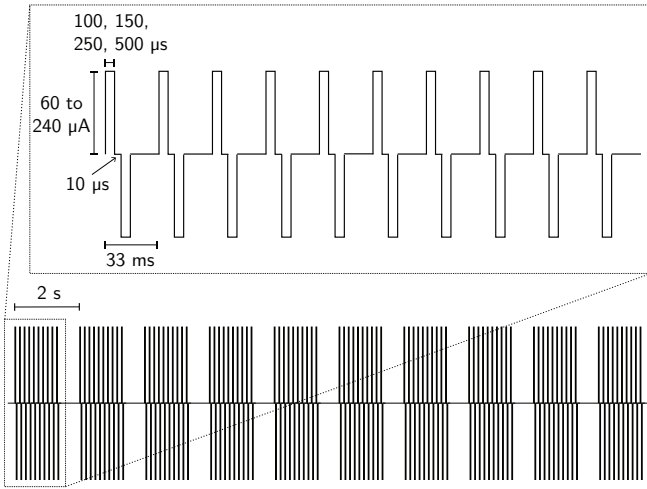


Figure 7. The stimulation sequence is composed of bursts of 10 pulses with a 33 ms period. The bursts are repeated 10 times with a 2 s period. This stimulation sequence is repeated for each combination of current (60 μA to 240 μA by steps of 20 μA) and phase duration (100 μs , 150 μs , 250 μs and 500 μs).

detecting activation by setting a threshold to the intensity within the area of each identified RGC at twice the standard deviation of the signal. The current threshold of each RGC is evaluated by fitting a sigmoid function to the neuron’s response, and selecting the amplitude associated to a detected response in 50 % of the cases. The data analysis is presented in detail in a separate paper [30].

3.2. Implant Power Budget

The implant power budget is determined by first characterizing the photovoltaic cell to determine its power output. Then, the remaining power for stimulation is evaluated by subtracting the implant standby power consumption from the photovoltaic cell output power. Then, from the calcium imaging experiments, the required stimulation power is measured at the average stimulation threshold for a single electrode. From this measurement, the maximum achievable number of stimulation pulses per second (maximum repetition rate) can be

determined given the available power.

3.2.1. Photovoltaic Cell Characterization

The photovoltaic cell is characterized by tracing the current-voltage and power-voltage curves under illumination with a 35 mW laser beam collimated on the photosensitive surface. The curves are traced with a Keithley 4200A source measurement unit (SMU).

3.2.2. Available Stimulation Power

The available stimulation power is derived from the implant power budget by subtracting the losses associated with the ocular medium, the photovoltaic cell and the implant standby power consumption from the 35 mW power source. The standby power consumption is measured via the voltage drop on a 10 Ω shunt resistor after the photovoltaic cell.

3.2.3. Maximum Repetition Rate

The maximum stimulation repetition rate is a key metric indicative of the capacity of the implant to eventually mimic neural code on a spike-by-spike basis [34]. This maximum rate is limited by the available power. To evaluate the maximum stimulation rate, the power consumption for a single electrode is measured while delivering a current at the average threshold required to elicit a response. The average thresholds are evaluated with calcium imaging for pulse widths of 100 μs , 150 μs , 250 μs , 500 μs with three different pieces of retina. Then, the maximum pulse rate that can be delivered on the array with the available power is estimated by dividing the available stimulation power by the power consumption for a single electrode. The result is then divided by the time slot duration (twice the pulse width plus a 10 μs interphase gap and a 30 μs calibration interval for balancing the currents of the anodic and cathodic phases).

4. Results

4.1. RGC Response to Wireless Stimulation

Firstly, the functionality of the device is verified by measuring the voltage waveform of a stimulation pulse with an oscilloscope (Figure 8).

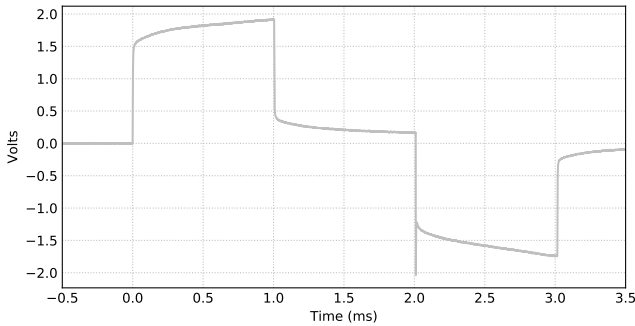


Figure 8. Voltage waveform of a 1 ms stimulation pulse at 100 μA in a physiological saline solution with an oscilloscope.

Figures 9 and 10 present the RGC spatial threshold maps from 100 μs and 500 μs pulses with the implant being powered by a 35 mW laser. In the threshold map, each circle represents one RGC, with the color indicating the threshold current. The RGCs that couldn't be activated with the maximum available current are shown as open circles. The blue square indicates the electrode position. As reported previously, 100 μs pulses lead to a more confined activation pattern. Using 500 μs pulses, the larger activation spread is most likely due to the unintended stimulation of the axon bundles passing the electrode and network-mediated stimulation via bipolar cells [30, 35].

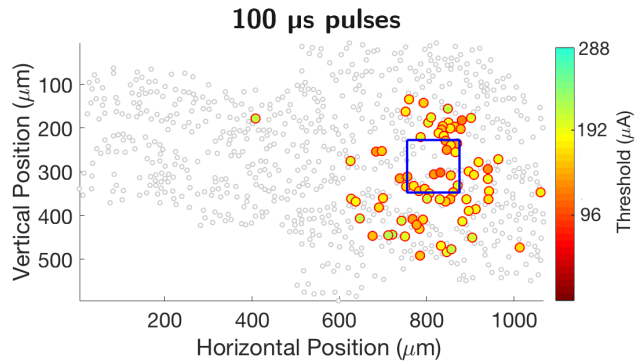


Figure 9. Spatial threshold map of retinal ganglion cells in a degenerate RCS rat retina for 100 μs biphasic charge-balanced stimulation pulses.

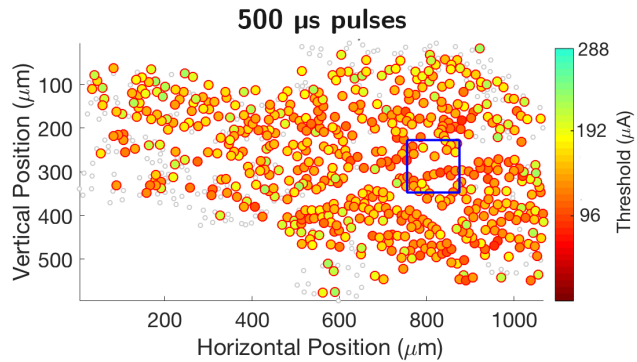


Figure 10. Spatial threshold map of retinal ganglion cells in a degenerate RCS rat retina for 500 μs biphasic charge-balanced stimulation pulses.

4.2. Implant Power Budget

4.2.1. Photovoltaic Cell Characterization To evaluate the power budget of the implant, the photovoltaic cell is first characterized. Figure 11 presents its current-voltage and power-voltage curves with a 35 mW laser. At peak power, the cell outputs 3.9 V with an efficiency of 59.4 %.

4.2.2. Available Stimulation Power The implant power budget following the photovoltaic cell characterization is presented in Table 1. With a maximum radiant power density of 4.06 mW/mm², a maximum of 36.5 mW can

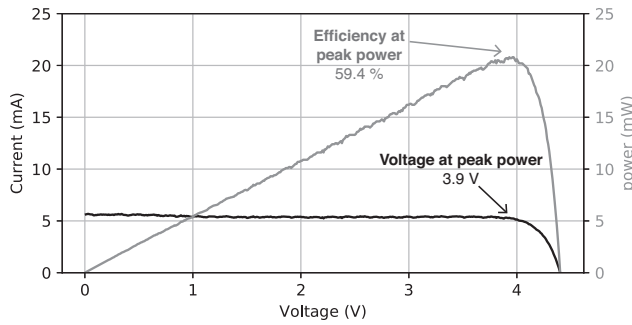


Figure 11. Photovoltaic cell characterization at 850 nm with a 35 mW beam collimated within the sensitive area. The efficiency peaks at 59.4 % at a voltage of 3.9 V.

enter the eye for a 9 mm^2 photovoltaic cell, assuming uniform light distribution. The laser power entering the eye is set slightly below 35 mW. Because of the light absorption of the ocular medium, 20 % of the light is absorbed (7.0 mW is dissipated), so that 28.0 mW reaches the photovoltaic cell [36]. The latter then converts the beam reaching its surface with an efficiency of 59.4 % (11.4 mW is dissipated). The ASIC consumes 3.5 mW of standby power consumption, which leaves 13.1 mW of power for delivering stimulation pulses.

Table 1. Implant Power Budget

Description	Power (mW)
Laser	35.0
Eye optical losses (20 % of 35 mW at 850 nm [36]).	-7.0
PV cell power dissipation (59.4 % of 28.0 mW)	-11.4
Implant standby power consumption	-3.5
Available stimulation power	13.1

4.2.3. Maximum Repetition Rate During stimulation, the power consumption depends on the current amplitude required to trigger action potentials, which varies according to many factors, including electrode-neuron distance, electrode size, neuron physiology and pulse characteristics. For the current

experiment conditions, the average thresholds for eliciting a response were calculated using calcium imaging for pulse widths of 100, 150, 250 and 500 μs . Then, the maximum current drawn from the ASIC is measured during pulse delivery, and subtracted from the standby power consumption. This current is then multiplied by the PV cell voltage to obtain the power consumption of a single electrode at the average stimulation threshold, as shown in Figure 12.

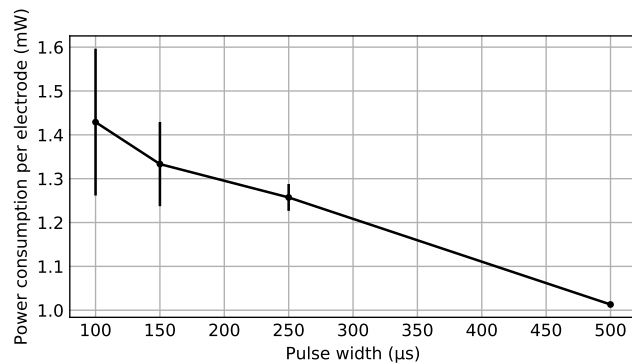


Figure 12. Power consumption of a single electrode at the average stimulation threshold for different pulse widths. The thresholds were averaged over three different retinas. The ASIC standby power consumption is excluded.

Figure 13 presents the expected maximum stimulation rate that can be delivered on the array for sequential stimulation based on the measured stimulation thresholds and available power.

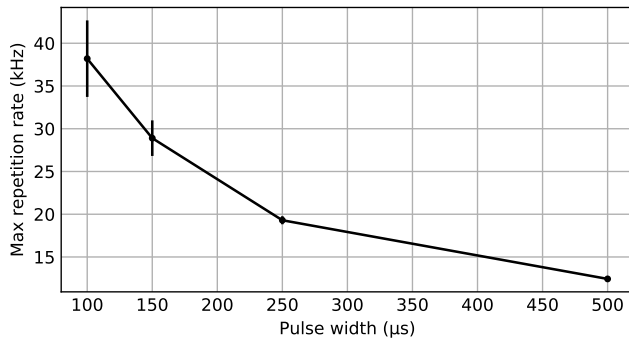


Figure 13. Maximum pulse rate that can be distributed on the electrode array based on the available power. It is calculated by dividing the available stimulation power (Table 1) by the power consumption per electrode (Figure 12). The result is then multiplied by the number of time slots per second. A time slot is equal to twice the pulse width plus 10 μ s for the interphase gap and 30 μ s for the current copying calibration phase.

5. Discussion

The main objective of the paper is to evaluate the possibility of wirelessly stimulating retinal ganglion cells using a CMOS stimulator ASIC powered by a photovoltaic cell. The results from the previous section suggest it is possible within certain limitations.

5.1. Safety of Near-Infrared Power Delivery

Figure 9 and 10 demonstrate that retinal ganglion cell response can be elicited using solely an infrared 35 mW laser beam as a power source. The 35 mW power source was chosen based on a photovoltaic cell with photosensitive dimensions of at least $3 \times 3 \text{ mm}^2$ in order to comply with the maximal safe irradiance of 4 mW/mm^2 at 850 nm. However, the prototype was realized with a commercially available $1.7 \times 1.7 \text{ mm}^2$ from Broadcom to reduce its development costs, as opposed to developing a cell with custom dimensions. Designing the implant with the appropriate photovoltaic

cell dimensions is critical to achieve safe irradiance levels.

Other implant architectures demonstrated the possibility of eliciting a response [7] with 0.2 to 10 mW/mm^2 of irradiance at 905 nm, but by targeting bipolar cell with a subretinal implant rather than retinal ganglion cells directly.

Different neural types respond very differently to electrical stimulation. Bipolar cells respond preferentially to longer pulse widths with low currents (around 25 ms) and retinal ganglion cells respond preferentially to shorter pulse widths with higher currents (around 0.1 ms) [30, 37, 38]. This leads to very different requirements in terms of stimulation strategies. When targeting bipolar cells, the longer pulse widths impose parallel stimulation strategies where most electrodes are activated simultaneously to achieve a reasonable refresh rate. Architectures based on photodiode arrays are well tailored to this approach, as each photodiode transduces the energy to the electrode to which they are coupled.

For retinal ganglion cells, the shorter pulse widths of around 0.1 ms allow for multiple time windows in which to deliver stimulation pulses within the image integration time of the brain [39]. Thus, electrodes could be stimulated sequentially, one at a time or in small groups. In terms of power delivery, this corresponds to concentrating the available power to the few simultaneously active electrodes. The photovoltaic cell approach proposed in this paper has the capacity of concentrating the total incident optical power on the active electrode, thus allowing shorter pulses at higher currents, as required for RGC stimulation.

5.2. Optimal pulse width considering the photovoltaic cell constraints

In order to achieve wireless operation, a retinal prosthesis must use a stimulation strategy that optimizes the power consumption. Although the instantaneous power consumption is higher for shorter pulse widths (Figure 12), the energy per pulse is lower (calculated by the multiplication of the power by the pulse duration). This is caused by the lower charge thresholds required to elicit a response with shorter pulse widths [40]. This effect is expected to plateau with pulse widths significantly below the cell chronaxie, at pulse widths around tens of microseconds [41].

Practically, other factors limit the delivery of really short pulses. Shorter pulses require larger currents to deliver comparable amounts of charge. However, stimulators have a limited maximum current, especially in the case of wirelessly powered devices where high peak currents require a large energy reservoir. Additionally, the compliance voltage of the stimulator limits the pulse widths. At shorter pulse widths, the higher currents induce larger access voltages caused by the resistive component of the electrode-electrolyte impedance. With the proposed implant, the ± 2.7 V compliance limit prevented reliable elicitation of a response with pulses below 100 μ s.

The reported experiments have demonstrated effective stimulation with a single electrode and with a power significantly below the available power from the photovoltaic cell. This leaves headroom for activating multiple electrodes simultaneously. Figure 13 presents the expected maximum repetition rate achievable given the experimental conditions. A higher repetition rate allows more accurate neural code reproduction in stimulation strate-

gies based on a rapid sequence of electrical stimuli from a given dictionary of possibilities [34]. To prevent electrical crosstalk during concurrent stimulation, these electrodes should be separated by a minimum distance, and ideally with return electrodes [42].

5.3. Experiment Limitations

In this experiment, the electrode array is located subretinally instead of epiretinally to preserve the line-of-sight between the RGCs and the confocal microscope objective lens. The electrodes are consequently separated from the RGCs by the thickness of the retina, which varies between 100 to 200 μ m. Additionally, the 120 μ m electrodes used in this experiment are relatively large compared to other experiments with electrode sizes as small as 5 μ m [43, 44]. These two factors increase the stimulation thresholds substantially. Alternatively, transparent indium tin oxide electrodes could be placed epiretinally without obstructing the line of sight [37], but would not exactly reproduce the behavior of the diamond electrode array. With smaller 10 μ m electrodes placed epiretinally, stimulating with biphasic electrical pulses of 0.05–0.1 ms result in thresholds in the order of 1 μ A [44, 45]. This requires close proximity of the electrodes to the ganglion cells, which is achievable in *in-vitro* experiments, but can be highly challenging in a clinical context [46, 47]. Lower thresholds would reduce the power consumption and allow higher stimulation repetition rates. Moreover, using smaller electrodes is critical to attain the spatial resolution required for single-cell stimulation and to reduce the required energy per stimulation pulse.

6. Conclusion

We presented an implant architecture based on an optical power and data link capable of wirelessly eliciting a response in retinal ganglion cells while retaining the flexibility of a stimulation controller. The limited permissible radiant power entering the eye is sufficient to power the stimulation ASIC, ancillary circuits and deliver stimulation pulses that elicit a response in retinal ganglion cells. The proposed solution promises higher safety and reliability due to the possibility of encapsulating the device in a hermetic package without wires protruding of the implant and through the eyeball. With the goal of achieving meaningful visual acuity gains, next generations of epiretinal prostheses will need to deliver stimulation pulses that reproduce the neural code at a spatial resolution of cellular scale. Towards that goal, one of the next major challenges will be the realisation of a closed-loop device capable of wirelessly stimulating and recording with high electrode density.

7. Acknowledgements

This research was supported by the Australian Research Council, through Linkage Grant LP160101052, Natural Sciences and Engineering Research Council of Canada (NSERC), through Collaborative Research and Development NSERC-CRD 530093 and by CMC microsystems. Authors gratefully acknowledge insightful discussions with Rob Hilkes, Tommy Rossignol, Émile Laplante, Patrice Buteau, Anne Bruneau and Jean Wilson.

8. Conflicts of Interest

SP is a shareholder in iBIONICS, a company developing a diamond based retinal implant.

SP and DG are shareholders and directors of Carbon Cybernetics, a company developing brain-machine neural interfaces.

References

- [1] Bourne R R A, Flaxman S R, Braithwaite T, Cicinelli M V, Das A, Jonas J B, Keeffe J, Kempen J H, Leasher J, Limburg H, Naidoo K, Pesudovs K, Resnikoff S, Silvester A, Stevens G A, Tahhan N and Wong T Y 2017 *The Lancet Global Health* **5** e888–e897 ISSN 2214109X
- [2] Da Cruz L, Coley B F, Dorn J, Merlini F, Filley E, Christopher P, Chen F K, Wuyyuru V, Sahel J, Stanga P, Humayun M, Greenberg R J and Dagnelie G 2013 *British Journal of Ophthalmology* **97** 632–636 ISSN 00071161
- [3] Stingl K, Bartz-Schmidt K U, Besch D, Chee C K, Cottrill C L, Gekeler F, Groppe M, Jackson T L, MacLaren R E, Koitschev A, Kusnyerik A, Neffendorf J, Nemeth J, Naeem M A N, Peters T, Ramsden J D, Sachs H, Simpson A, Singh M S, Wilhelm B, Wong D and Zrenner E 2015 *Vision Research* **111** 149–160 ISSN 18785646
- [4] Humayun M S, Dorn J D, Da Cruz L, Dagnelie G, Sahel J A, Stanga P E, Cideciyan A V, Duncan J L, Elliott D, Filley E, Ho A C, Santos A, Safran A B, Arditi A, Del Priore L V and Greenberg R J 2012 *Ophthalmology* **119** 779–788 ISSN 01616420
- [5] Ho A C, Humayun M S, Dorn J D, da Cruz L, Dagnelie G, Handa J, Barale P o, Sahel J A, Stanga P E, Hafezi F, Safran A B, Salzmann J, Santos A, Birch D, Spencer R, Cideciyan A V, de Juan E, Duncan J L, Elliott D, Fawzi A, Olmos de Koo L C, Brown G C, Haller J A, Regillo C D, Del Priore L V, Arditi A, Gerasch D R, Greenberg R J and Argus II Study Group 2015 *Ophthalmology* **122** 1547–54 ISSN 1549-4713
- [6] Daschner R, Greppmaier U, Kokelmann M, Rudolf S, Rudolf R, Schleeauf S and Wrobel W G 2017 *Biomedical Microdevices* **19** 1–8 ISSN 15728781
- [7] Mathieson K, Loudin J, Goetz G, Huie P, Wang L, Kamins T I, Galambos L, Smith R, Harris J S, Sher A and Palanker D 2012 *Nature Photonics* **6** 391–397 ISSN 1749-4885
- [8] Boinagrov D, Lei X, Goetz G, Kamins T I, Mathieson K, Galambos L, Harris J S and Palanker

- D 2016 *IEEE Transactions on Biomedical Circuits and Systems* **10** 85–97 ISSN 19324545
- [9] Palanker D, Huie P, Vankov A, Asher A and Baccus S 2005 *Progress in Biomedical Optics and Imaging - Proceedings of SPIE* **5688** 1–11 ISSN 16057422
- [10] Paraskevoudi N and Pezaris J S 2019 *Frontiers in Systems Neuroscience* **12** 1–21
- [11] Asher A, Segal W A, Baccus S A, Yaroslavsky L P and Palanker D V 2007 *IEEE Transactions on Biomedical Engineering* **54** 993–1004 ISSN 00189294
- [12] Jensen R J and Rizzo J F 2006 *Experimental Eye Research* **83** 367–373 ISSN 00144835
- [13] Greenwald E, Maier C, Wang Q, Beaulieu R, Etienne-Cummings R, Cauwenberghs G and Thakor N 2017 *IEEE Transactions on Biomedical Circuits and Systems* **11** 324–335 ISSN 1932-4545
- [14] Sooksood K, Stieglitz T and Ortmanns M 2010 *IEEE Transactions on Biomedical Circuits and Systems* **4** 162–170 ISSN 1932-4545
- [15] Jepson L H, Hottowy P, Mathieson K, Gunning D E, Dabrowski W, Litke A M and Chichilnisky E J 2014 *Journal of Neuroscience* **34** 4871–4881 ISSN 15292401
- [16] Matteucci P B, Chen S C, Tsai D, Dodds C W D, Dokos S, Morley J W, Lovell N H and Suaning G J 2013 *Investigative Ophthalmology and Visual Science* **54** 4307–4320 ISSN 01460404
- [17] Fan V H, Grosberg L E, Madugula S S, Hottowy P, Dabrowski W, Sher A, Litke A M and Chichilnisky E 2019 *Journal of Neural Engineering* **16** 025001 ISSN 1741-2560
- [18] Lemaire W, Benhouria M, Koua K, Besrou M, Gauthier L P, Martin-Hardy G, Roy S and Fontaine R 2020 *IEEE Journal of Solid-State Circuits (submitted)*
- [19] Delori F C, Webb R H and Sliney D H 2007 *Journal of the Optical Society of America A* **24** 1250 ISSN 1084-7529
- [20] Laser Institute of America 2007 American National Standard for Safe Use of Lasers Tech. rep.
- [21] Fafard S, York M C, Proulx F, Valdivia C E, Wilkins M M, Arès R, Aimez V, Hinzer K and Masson D P 2016 *Applied Physics Letters* **108** ISSN 00036951
- [22] Mashhadi I A, Pahlevani M, Hor S, Pahlevani H and Adib E 2019 *IEEE Transactions on Power Electronics* **34** 6425–6439 ISSN 08858993
- [23] Chen K, Yang Z, Hoang L, Weiland J, Humayun M and Liu W 2010 *IEEE Journal of Solid-State Circuits* **45** 1946–1956 ISSN 0018-9200
- [24] Hosung Chun, Yuanyuan Yang and Lehmann T 2014 *IEEE Transactions on Biomedical Circuits and Systems* **8** 108–118 ISSN 1932-4545
- [25] Tran N, Bai S, Yang J, Chun H, Kavehei O, Yang Y, Muktamath V, Ng D, Meffin H, Halpern M and Skafidas E 2014 *IEEE Journal of Solid-State Circuits* **49** 751–765 ISSN 0018-9200
- [26] Slavcheva E, Vitushinsky R, Mokwa W and Schnakenberg U 2004 *Journal of the Electrochemical Society* **151** 226–237 ISSN 00134651
- [27] Ahnood A, Meffin H, Garrett D J, Fox K, Ganesan K, Stacey A, Apollo N V, Wong Y T, Lichter S G, Kentler W, Kavehei O, Greferath U, Vessey K A, Ibbotson M R, Fletcher E L, Burkitt A N and Prawer S 2017 *Advanced Biosystems* **1** 1600003 ISSN 23667478
- [28] Ganesan K, Garrett D J, Ahnood A, Shivdasani M N, Tong W, Turnley A M, Fox K, Meffin H and Prawer S 2014 *Biomaterials* **35** 908–915 ISSN 01429612
- [29] Garrett D J, Ganesan K, Stacey A, Fox K, Meffin H and Prawer S 2012 *Journal of Neural Engineering* **9** ISSN 17412560
- [30] Tong W, Stamp M, Apollo N, Ganesan K, Meffin H, Prawer S, Garrett D J and Ibbotson M 2019 *Journal of neural engineering* ISSN 1741-2552
- [31] Mercier P P, Bandyopadhyay S, Lysaght A C, Stankovic K M and Chandrakasan A P 2014 *IEEE Journal of Solid-State Circuits* **49** 1463–1474 ISSN 00189200
- [32] Dorn J D, Ahuja A K, Caspi A, Da Cruz L, Dagnelie G, Sahel J A, Greenberg R J and McMahon M J 2013 *JAMA Ophthalmology* **131** 183–189 ISSN 21686165
- [33] Ray A, Sun G J, Chan L, Grzywacz N M, Weiland J and Lee E J 2010 *Cell and Tissue Research* **339** 481–491 ISSN 0302766X
- [34] Shah N P, Madugula S, Grosberg L, Mena G, Tandon P, Hottowy P, Sher A, Litke A, Mitra S and Chichilnisky E J 2019 *International IEEE/EMBS Conference on Neural Engineering, NER 2019-March* 714–718 ISSN 19483554
- [35] Chang Y C, Ghaffari D H, Chow R H and Weiland J D 2019 *Journal of Neural Engineering* **16** 0–14 ISSN 17412552
- [36] Boettner E A 1962 *Investigative Ophthalmology and Visual Science* **1** 776–783 ISSN 1552-5783
- [37] Weitz A C, Nanduri D, Behrend M R, Gonzalez-

- Calle A, Greenberg R J, Humayun M S, Chow R H and Weiland J D 2015 *Science Translational Medicine* **7** 318ra203–318ra203 ISSN 1946-6234
- [38] Freeman D K, Eddington D K, Rizzo J F and Fried S I 2010 *Journal of Neurophysiology* **104** 2778–2791 ISSN 0022-3077
- [39] Chichilnisky E J and Kalmar R S 2003 *Journal of Neuroscience* **23** 6681–6689 ISSN 02706474
- [40] Boinagrov D, Loudin J and Palanker D 2010 *Journal of Neurophysiology* **104** 2236–2248 ISSN 00223077
- [41] Merrill D R, Bikson M and Jefferys J G 2005 *Journal of Neuroscience Methods* **141** 171–198 ISSN 01650270
- [42] Flores T, Goetz G, Lei X and Palanker D 2016 *Journal of Neural Engineering* **13** ISSN 17412552
- [43] Hottowy P, Skoczeń A, Gunning D E, Kachiguine S, Mathieson K, Sher A, Wiącek P, Litke A M and Dąbrowski W 2012 *Journal of Neural Engineering* **9** 066005 ISSN 1741-2560 (Preprint NIHMS150003)
- [44] Sekirnjak C, Hottowy P, Sher A, Dabrowski W, Litke A M and Chichilnisky E J 2006 *Journal of Neurophysiology* **95** 3311–3327 ISSN 0022-3077
- [45] Grosberg L E, Ganesan K, Goetz G A, Madugula S S, Bhaskhar N, Fan V, Li P, Hottowy P, Dabrowski W, Sher A, Litke A M, Mitra S and Chichilnisky E J 2017 *Journal of Neurophysiology* **118** 1457–1471 ISSN 15221598
- [46] Gregori N Z, Callaway N F, Hoepfner C, Yuan A, Rachitskaya A, Feuer W, Ameri H, Arevalo J F, Augustin A J, Birch D G, Dagnelie G, Grisanti S, Davis J L, Hahn P, Handa J T, Ho A C, Huang S S, Humayun M S, Iezzi R, Jayasundera K T, Kokame G T, Lam B L, Lim J I, Mandava N, Montezuma S R, Olmos de Koo L, Szurman P, Vajzovic L, Wiedemann P, Weiland J, Yan J and Zacks D N 2018 *American Journal of Ophthalmology* **193** 87–99 ISSN 00029394
- [47] Ahuja A K, Yeoh J, Dorn J D, Caspi A, Wuyyuru V, McMahon M J, Humayun M S, Greenberg R J, DaCruz L and Argus II Study Group 2013 *Translational Vision Science & Technology* **2** 1 ISSN 2164-2591